This is a preprint, the final version is subject to change, of the American Mineralogist (MSA)
Cite as Authors (Year) Title. American Mineralogist, in press.
(DOI will not work until issue is live.) DOI: http://dx.doi.org/10.2138/am-2017-5664

Revision 5

Polarized FTIR spectroscopic examination on hydroxylation in the minerals of the wolframite group, $(Fe,Mn,Mg)[W,(Nb,Ta)][O,(OH)]_4$

Dominik Talla[1,2,*], Anton Beran[1], Radek Škoda[2], Zdeněk Losos[2]

[1] Institut für Mineralogie und Kristallographie, Universität Wien, Althanstraße 14, 1090 Wien, Austria

[2] Department of Geological Sciences, Masaryk University, Kotlářská 2, 611 37 Brno, Czech Republic

[*] corresponding author

Abstract

Polarized FTIR spectroscopic measurements of eleven natural wolframite single crystals from different occurrences revealed the common presence of structurally bound OH groups in their crystal lattice, with potential influence on the properties of these geologically and technologically important group of compounds. Despite differences in the appearance of the OH absorption pattern, dependent among other on the endmember ratio, two types of 'intrinsic' OH defects could be discerned from detailed studies of the pleochroic behavior of the absorption bands both at 80 K and room temperature. The accompanying chemical analyses by the electron microprobe helped to clearly identify the substitution trend $W^{6+} + O^{2-} \leftrightarrow (Nb,Ta)^{5+} + OH^-$ as the prevailing

hydrogen incorporation mechanism into wolframite. The assignment of the observed IR absorption phenomena to hydrous defects was confirmed by the results of deuteration experiments and the negligible contribution of included impurities to the FTIR spectra in the OH absorption region. The results obtained in this study of natural wolframite crystals can be used to detect and analyze hydrous defects in synthetic technologically important tungstates.

Keywords: Wolframite, FTIR spectroscopy, OH defects, nominally anhydrous minerals, deuteration, flux synthesis

Introduction

Wolframite group minerals, $M^{2+}WO_4$ (M^{2+} = Fe, Mn, Mg, Zn) present – besides scheelite, $CaWO_4$ – the most important tungsten ore mineral group. They typically occur within hydrothermal veins that are associated with granitic stocks or batholiths, forming sometimes deposits with unconventionally high ore grades. Due to its high specific gravity, hardness and resistance to weathering, wolframite also occurs in eluvial placer deposits (Wei et al. 2012; Jingwen et al. 2013). Chemically it forms a solid solution between two dominant endmember compositions - $FeWO_4$ (ferberite) and $MnWO_4$ (hübnerite). Sporadically, Zn forms an essential component, thus providing the mineral sanmartinite, $ZnWO_4$. As an exceptional case, magnesium-dominant wolframite (huanzalaite) with a $MgWO_4$ fraction of 58 mol% has been reported by Ferenc and Uher (2007) from the Rochovce granite exocontact, Ochtinná, Slovakia. Contents of up to 5 mol% have been measured in samples from metagreisens occurring near Humpolec, Czech Republic, by Losertová et al. (2012, 2013, 2014) and confirmed in this study

(samples CET and OLH). Miyawaki et al. (2010) described huanzalaite, $MgWO_4$, as a new mineral species, containing (besides Fe and Mn) a maximum $MgWO_4$ component of 89 mol%.

Wolframite also belongs to the group of artificially produced tungstates which have gained, due to their semi-conducting behavior (Guha Thakurta and Dhutta 1980) and antiferromagnetic properties dictated in part by the endmember ratio (Guillen and Regnard 1985; Lalić et al. 2011), considerable technical interest in view of their potential technological significance in magnetoelectronic and photochemical industry (Redfern et al. 1995).

The monoclinic crystal structure of wolframite shows some similarity in atomic coordination and polyhedral linkage to the orthorhombic α-PbO_2 structure, but is more closely related to minerals belonging to the monoclinic orthorhombic samarskite-(Y), $(Y,Fe^{3+})(Nb,Ta)O_4$ and to the orthorhombic columbite group, $(Fe^{2+},Mn,Mg)(Nb,Ta)_2O_6$. In this manner, wolframite is also structurally similar to brookite, presenting the orthorhombic modification of TiO_2, where the presence of OH defects has been reported by Beran and Zemann (1971). A characteristic ore microscopic feature of wolframite is the appearance of red internal reflections, which indicates its transparency already on the border between visible and the near-infrared (< 15000 cm^{-1}) spectral ranges.

Infrared (IR) spectroscopy is a sensitive method for detecting trace hydrogen bound to oxygen atoms, thus forming OH or H_2O defects in the structure of nominally anhydrous minerals (Johnson 2006; Libowitzky and Beran 2006; Rossman 2006). The pleochroic scheme of the absorption bands in polarized IR spectra provides information on the orientation of the hydrous species; the band position suggests a certain O-H···O bond length and the band intensity provides information on the hydrogen concentration. This method also is a useful tool for the identification of extremely fine-grained hydrous and/or hydroxyl mineral phases included in the host mineral, which contribute to the overall stretching OH absorption pattern.

While it is now well established that 'hydrous defects' commonly occur in nominally anhydrous silicate minerals, there are comparatively few studies on the H_2O content of nominally anhydrous non-silicate phases; hydrous defects have been described in baryte (Beran et al. 2010), xenotime (Talla et al. 2011), triphylite (Libowitzky et al. 2012) and wulfenite (Talla et al. 2013). This study of wolframite presents an exceptional case where the presence of hydrogen traces has been established in an opaque ore mineral phase by using polarized IR spectroscopy. The principal aim of the present paper is to characterize the absorption properties of wolframite in the OH stretching vibrational region and to discuss plausible models for the incorporation of a hydrous phase into the structure of this important tungsten ore mineral.

Experimental

Sample description and sample preparation

Eleven single crystals of wolframite with varying chemical composition from different localities and their main parameters are summarized in Table 1; six samples are dominated by the hübnerite component, and five samples by the ferberite component. In addition, three synthetic single crystals of $MgWO_4$, $MnWO_4$ and $FeWO_4$ were used as reference samples for the spectroscopic analyses. Under a reflected-light microscope and a scanning electron microscope, small parts of the oriented polished crystal slabs were of gemmy quality, without included foreign phases. The crystal slabs, further checked for chemical homogeneity using the electron microprobe, revealed significant chemical zoning in the natural samples.

The selected single crystals were oriented by X-ray single-crystal diffraction using a Nonius Kappa CCD four-circle diffractometer. In two sequences of preparation, two crystal slabs

were prepared, one slab polished parallel to (010) and a second slab polished parallel to (100). The Miller indices refer to the monoclinic space group P2/c, a ~ 4.8, b ~ 5.7, c ~ 5.0 Å, β ~ 91°, (Cid-Dresdner and Escobar 1968; Weitzel 1976). The thickness of the crystal plates was 200 μm for the most strongly absorbing samples and up to 290 μm for those with weaker OH-stretching IR absorption. The polished slabs were prepared by grinding with SiC grit 1000 abrasive on glass, and polishing with 6, 1, and 0.25 μm diamond pastes on nylon cloth. The preparation of the polished section of the synthetic phases followed the same polishing procedure.

Synthesis of $MgWO_4$, $MnWO_4$ and $FeWO_4$ crystals

Pure $MgWO_4$, $MnWO_4$ and $FeWO_4$ crystals were prepared by means of the flux method, which ensures none or a negligibly small amount of hydrous species incorporated in the structure. The flux consisted of a mixture of 5 g of sodium polytungstate ($Na_6[H_2W_{12}O_{40}]$) with 1 g of $NaHCO_3$. The reason for the $NaHCO_3$ addition was to calibrate the molar ratio Na:W roughly to 1:1, preventing the formation of large insoluble euhedral WO_3 crystals, observed in the initial experiments.

The respective M^{2+}-cation (M^{2+} = Fe, Mn, Mg) was admixed to the flux as 2 g of the corresponding M^{2+}-nitrate hydrate; $Fe(NO_3)_2 \cdot 9H_2O$ for ferberite, $Mn(NO_3)_2 \cdot 4H_2O$ for hübnerite and $Mg(NO_3)_2 \cdot 6H_2O$ for huanzalaite, respectively. The mixture to obtain $MgWO_4$ was placed into a 50 mL Pt-crucible. To prevent Fe-oxidation during the $FeWO_4$ synthesis, a graphite crucible inserted into a baked fireclay container to avoid spills had to be used to ensure sufficient reducing conditions. $MnWO_4$ was synthesized in a 50 mL Ni-crucible along with coke present in the furnace to provide a reducing CO atmosphere. The filled vessels were heated at a rate of 270 °C/h to a peak temperature of 1100 °C. Following a soaking phase of 3 h, the temperature was reduced to 700 °C at a rate of 4.5 °C/h. Afterwards, the samples were left in the furnace to cool

down spontaneously to room temperature. The flux was then easily dissolved in a 1 *M* aqueous solution of NaOH after approximately 20 h of immersion time, allowing easy removal of the elongated tabular or straw-like crystals.

Despite our effort, Fe^{2+} oxidized partly to the trivalent state. This caused the formation of large olive-green straw-like crystals of a compound identified as $NaFe^{3+}(WO_4)_2$ instead of ferberite, $FeWO_4$.

IR spectroscopy

Polarized single-crystal IR spectra were measured with a Bruker Hyperion 1000 microscope (LN_2-cooled MCT detector) attached to a Bruker FTIR spectrometer Tensor 27 (Globar light source and equipped with a KRS-5 grid polarizer). The instrumental spectral resolution was 4 cm^{-1}, the lateral spatial resolution was 50 µm; spectra were averaged over 120 scans. IR spectra were recorded at room temperature as well as at 80 K. A Linkam FTIR 600 heating/cooling stage was used to provide low-temperature conditions.

Deconvolution of the OH absorption patterns into single absorption peaks was performed by the program 'PeakFit' (Jandel Scientific), using a Voigt peak-shape function (superposition of Lorentzian and Gaussian functions with independently variable full widths at half maximum (FWHMs)). The overall standard fitting error between the model and the measured data, used for the calculation of the H_2O contents, ranges to $r^2 = 0.05$ at worst. Test measurements from areas with clearly visible cracks and inclusions showed that the only background artefact consists of a broad H_2O band centred at 3400 cm^{-1}, with a high-energy shoulder near 3600 cm^{-1}. Since this band was easily recognizable in the spectra, it was used as an indicator for the presence of submicroscopic, hardly visible cracks and phase inclusions. Special care was taken to exclude such spacial areas from further analyses.

While the relative water contents are well internally consistent given the overall goodness of fit, a significant source of error as to the calculation of absolute H_2O contents is the method of estimating the integrated molar absorption coefficient in the case of nominally anhydrous minerals (Koch-Müller and Rhede 2010).

Absorption figures on (010) and (100) crystal slabs were obtained after rotation of the polarizer over the range of 180° by steps of 15°. The IR spectra and the absorption figures are displayed as linear absorption coefficients α in cm^{-1}; α is defined as A/t, where A is the linear absorbance $\log(I_0/I)$ and t is the thickness of the crystal slab measured in cm.

Heating and deuteration experiments

The deuteration experiments on broken-off sections of the wolframite slabs consisted of warming up the material to the peak temperature in air with a rate of 1 °C/min in a Nabertherm N11/H muffle furnace. Peak temperatures progressing in 100°C steps from 200°C to 500 °C were used, the holding time was 25 h. Following each step, the IR spectra were measured at room temperature immediately after cooling down.

The deuteration experiments were performed following the procedure described by Ryskin (1974). Parts of the wolframite #5730 crystal slab were placed in a steel autoclave (inner volume 2 cm^3), containing 1 cm^3 D_2O and held at a peak temperature of 360 °C for 72 h. The deuteration of pure hübnerite, requiring a much higher temperature, was performed by inserting part of the #1345 crystal slab contained in a Pt-vessel along with a D_2O-filled quartz glass container into a cork-sealed glass tube. The apparatus was heated by a gas flame to 600 °C for 16 h, exposing the sample to a D_2O-saturated atmosphere during this entire time. As for heating runs, FTIR spectra of the samples prior and following deuteration were acquired at room temperature.

Chemical analyses

The chemistry of the wolframite single crystals was inspected and analyzed by a Cameca SX 100 electron microprobe (EMP) at an operating voltage of 15 kV, 20 nA sample current, 3 μm beam size and counting times of 20. The EMP analyses were performed at the center of the spots (diameter ~ 50 micrometers) examined by IR spectroscopy. It was further assumed the 50-micron areas from which the IR spectra were collected, were chemically homogeneous. The following standard materials were used: almandine for Fe, tephroite for Mn, spinel for Mg, columbite for Nb, CrTa2O6 for Ta, sanidine for Si, anatase for Ti and metallic W for W; the analytical data were PAP corrected. EMP analyses of the eleven samples are presented in Table 2. A JSM-6400 scanning electron microscope (SEM) equipped with a Link energy dispersive X-ray system was used for sample surface imaging and identification of included impurities. By applying an acceleration voltage of 15 kV, a magnification of up to 3000x was obtained.

Quantitative IR spectroscopic 'water' determination

The integrated absorbance values A_i (cm^{-1}) at room temperature, measured parallel and perpendicular to the direction of the maximum absorbance on the (010) slab and parallel to [010] on the (100) slab, were summed up to get the total integrated absorbance value $A_{i\,tot}$, which was used for the calculation of the integrated absorption coefficient α_i (cm^{-2}; $\alpha_i = A_{i\,tot}/t$). As expressed by the Beer's law, α_i is directly related to the concentration c (mol L^{-1}) via the integrated molar absorption coefficient ε_i (L mol^{-1}_{H2O} cm^{-2}). The hydroxyl content, calculated as H_2O in wt% is determined using the relationship $c_{H2O} = (1.8/D)\,(\alpha_i/\varepsilon_i)$, where D is the density of the mineral (7.45 g/cm^3 was chosen as a constant value) (Beran et al. 1993; Libowitzky and Rossman 1996; Libowitzky and Beran 2004). The ε_i value was derived from the linear calibration curve of Libowitzky and Rossman (1997) correlating the integrated molar absorption coefficient

of the OH stretching vibration vs. the wavenumber (Paterson's 1982 method). As discussed below, (semi-) quantitative data on the water content can be obtained more easily from polarized measurements performed solely parallel to the direction of maximum absorbance on the frequently observed (010) cleavage face.

Results

Chemical composition (EMP and SEM data)

Analytical EMP data of the studied natural crystals are summarized in Table 2. The samples #1318, #5735, #5725 and #5730 show a similar composition, dominated by a hübnerite component of about 60 mol%. The samples #5721 and #1345 represent hübnerite crystals with pure endmember composition. The samples #5737, #797, CET, OLH and #12767 are dominated by the ferberite component; #5737 and #12767 come relatively close to the ferberite endmember composition. The ferberite-dominating samples #5737, CET and OLH reveal a significant huanzalaite component (Table 2). Except in the samples #1345 and OLH, Nb_2O_5 contents are detectable in considerable amounts, reaching 1.45 wt% in sample #5730 (with the standard measurement error of 0.15 wt%). The maximum Ta_2O_5 content amounts to 0.21 wt% and also occurs in sample #5730 (with the standard measurement error up to 0.05 wt%) . In samples #5737, #5721, #1345, CET, OLH and #12767 the Ta_2O_5 contents are below the detection limit.

W shows a clear negative correlation with Nb and Ta in a molar exchange ratio almost precisely equal to 1:1 (Fig. 1). The amounts of the latter two elements correlate positively with one another, in accordance with their general geochemical behavior within the continental crust (Rudnick and Gao 2004).

Scanning electron microscopy (SEM) reveals tiny veinlets of scheelite as included mineral phases in the hübnerite sample #1345. Stolzite occurs in form of veinlets and as tiny (hyp-) idiomorphic mineral inclusions in the ferberite sample #5730.

IR spectra of wolframite

Polarized OH absorption spectra of selected wolframite samples with different chemical compositions and from different localities, measured on (010) plates with the electric vector **E** of the polarized IR radiation vibrating parallel to the direction of maximum absorbance, are shown in Fig. 2. The OH-stretching absorption region in the IR spectra of the various wolframite crystals contains two apparent groups of absorption bands, one centred around 3400 cm^{-1} and the other at 3100 cm^{-1}. The relative intensities of the two main absorption groups varies within the same sample, as can be seen e.g. along a profile in the sample #5725 (Fig. 3), pointing to the uneven spatial distribution of the OH groups. The FWHM of the bands constituting the band groups also varies strongly between the samples. For example, the hübnerite-dominating wolframite #5730 shows two relatively broad and strong absorption humps (one for each band group) at room temperature, with splitting into the constituent bands visible only after cooling the crystal down to 80 K (Fig. 4). In contrast, it is typical of pure hübnerite end members, represented by samples #1345 and #5721, to show the bands well resolved even at room temperature (Fig. 2).

The spectral range of OH stretching measured at room temperature as well as at 80 K was decomposed by fitting the minimum number of Voigt-shaped components needed to describe the experimental profile. For pure hübnerite (samples #1345 and #5721), a baseline correction has been applied in the 3600-3000 cm^{-1} region. Figures 5 and 6 present the polarized spectra of samples #1318 and #1345, respectively, both measured on (010) slabs parallel to the direction of maximum absorbance and parallel to the direction of the *c* axis. Measurements with **E** vibrating

parallel to the *b* axis have been performed on (100) slabs. The spectra of sample #1318 exhibit a high-energetic band group with two bands at 3420 and 3360 cm^{-1}, as well as a low-energetic band group consisting of five bands at 3230, 3130, 3040, 2960 and 2870 cm^{-1}. The last three low-energetic bands seem to be overlapped by extra bands, which are most probably due to trace amounts of contaminating hydrocarbons. The deconvoluted spectrum of pure hübnerite (see Fig. 6) reveals more bands at somewhat different wavenumbers and with different band shapes. In analogy, the high-energetic band group is dominated by a sharp band at 3370 cm^{-1} and weak satellite bands at 3430, 3390 and 3340 cm^{-1}. The low-energetic band group consists of bands at 3240, 3150, 3080 and 2980 cm^{-1}. Somewhat elevated background is compensated by fitting an additional broad band at 3260 cm^{-1}.

Heating experiments performed on crystal slabs of sample #5730 ($Fb_{38}Hb_{62}$) indicate significant differences in the decrease of OH band intensities with increasing temperature. The low-energetic band group in the 3230-2870 cm^{-1} region starts to decrease in intensity at 250 °C, whereas the high-energetic band group with bands at 3420 and 3360 cm^{-1} at 350 °C. This indicates a somewhat higher thermal stability of the higher energetic band group. Both band groups decrease continuously in intensity at further heating up to 400 °C. Upon annealing at 500 °C for 36 h, both band groups disappear. Pure hübnerite (sample #1345) lost all its OH bands after heating the sample to 350 °C for 72 h.

As shown in Fig. 7a, deuteration experiments performed at 360 °C for 72 h on crystal slabs of the sample #5730 produce absorption bands at 2520 and 2320 cm^{-1}, which are due to OD stretching vibrations. These two bands are the OD equivalents of the high- and low-energetic OH band groups with absorption maxima around 3400 and 3100 cm^{-1}. The resulting OH/OD wavenumber factor of 1.35 perfectly agrees with the theoretical value. Deuteration of pure hübnerite crystals (sample #1345) performed at 600 °C for 16 hours produced absorption bands at

2525 and 2495 cm^{-1} with a complete replacement of the original OH bands (Fig. 7b). The OH/OD factor of 1.35 perfectly matches the wavenumber ratio between the OD band at 2495 cm^{-1} and the corresponding dominant OH band at 3370 cm^{-1}. The deuteration applied to hübnerite gave rise to an additional high-energetic OD band at 2525 cm^{-1} which apparently coincides with the OD band at 2520 cm^{-1} in sample #5730, and it is thus attributed to the OD equivalent of the OH band at 3420 cm^{-1}. As can be seen in Fig. 6, a weak high-energetic satellite band at 3430 cm^{-1} is indeed developed also in pure hübnerite.

Fig. 8a and 8b present OH absorption figures measured at room temperature on (010) and (100) plates of the samples #5730 and #1345, respectively. As all bands measured on one crystal plate have the same pleochroic behavior, only three selected absorption figures of the strongest OH bands, at best resolved from the others (lowest overlaps, small fitting error) are shown. The high-energetic band group in ferberite is represented by the absorption figure of the band at 3420 cm^{-1}, the low-energetic band group by the absorption figures of bands at 3230 and 3130 cm^{-1}. In sample #1345 the high-energetic band group is represented by the absorption figures of the bands at 3370 and 3340 cm^{-1} and the low-energetic band group by the absorption figure of the band at 3240 cm^{-1}. The high- and low-energetic band groups of sample #5730 and also of sample #1345 show maximum absorption in (010) when the electric vector **E** of the polarized radiation vibrates parallel to a direction which is tilted by an angle of about 110° from the *c* axis, thus coming near the direction of the *a* axis. In (100) the band groups of sample #5730 have a somewhat less pronounced pleochroism in comparison with pure hübnerite, such as samples #1345 and #5721. However, both minerals have an essentially stronger absorption when **E** vibrates parallel to the *b* axis than parallel to the *c* axis (Fig. 8).

H_2O content of wolframite (IR spectroscopic determination)

The averaged water contents of wolframites from the different localities are summarized in Table 1. As discussed below, under the assumption of two types of structural OH groups, the H_2O I water contents are related to the high-energetic bands and the H_2O II water contents to the low-energetic bands. Assuming mean wavenumbers of 3400 cm^{-1} for the high-energetic bands and 3100 cm^{-1} for the low-energetic bands, the ε_i values derived from the linear calibration curve of Libowitzky and Rossman (1997), amount to 87050 and to 161030 L mol^{-1}_{H2O} cm^{-2}, respectively. The total H_2O contents range from 74 (sample OLH) to 448 wt.ppm (sample #797). The high-energetic band group of sample #5730 represents the highest observed H_2O I content, namely 233 wt.ppm. The sample #797 shows, with 288 wt.ppm, the highest H_2O II content corresponding to the low-energetic band group.

The monoclinic crystal system of wolframite renders polarized measurements parallel to different crystallographic directions inconvenient, requiring two sections of the particular crystal to obtain the exact value of the total integrated absorption coefficient α_{tot}, necessary to calculate the H_2O content. The required use of two different crystal slabs excludes the possibility to conduct measurements along the three principle optical directions on the very same crystal. Therefore, a method is required to assess the value of the total integrated absorption coefficient in an optically biaxial mineral from a single slab, by determining a scaling factor between the integrated absorption coefficient observed along a certain crystallographic direction in but one of the slabs (α_i), and using a scaling factor to recalculate it to the total integrated absorption coefficient α_{tot} – the 'short' method' (Bell et al. 2004; Beran et al. 2010). With **E** vibrating perpendicular to the *c* axis in the (010) slab, all OH absorption bands display nearly maximum absorption. Therefore, this direction was selected to acquire the reference values α_i for H_2O I and H_2O II.

By multiplying the integrated absorption coefficient α_i reference value of the 3400 cm^{-1} band group by a factor of 2.3 and the α_i reference value of the 3100 cm^{-1} band group by a factor of 2.1, the total integrated absorption coefficient (α_{tot}) values for H_2O I and H_2O II, respectively, could be obtained (Fig. 8). The values of the two factors were derived from the full evaluation of the pleochroic scheme of the OH absorption bands measured on (010) and (100) crystal plates of the samples #5730, #1318 (whose absorption pattern matches by character the broad humps seen in Fe-containing samples) and #1345.

Despite the significant difference in measured sample volume and a certain degree of mismatch between the placement of FTIR and EMP measurements into the same points, important correlation trends between the chemical composition of the samples and the distribution of hydrous defects have been revealed. The OH defect corresponding to the high-energy band group, H_2O I, shows a strong positive correlation with the sum of Nb_2O_5 and Ta_2O_5 contents (Fig. 9), while H_2O II, corresponding to the low-energy band group, does not exhibit any correlation with the amount of Nb and Ta. It should be noted that neither H_2O I nor H_2O II show correlation with the content of Fe, Mn, and Mg.

Discussion

Based on observations under the reflected-light microscope with an actual total magnification of up to 500x and observations made by using a scanning electron microscope (SEM) for sample surface imaging with a magnification of up to 3000x, we found no indications for the presence of oriented intergrown submicroscopic hydrous mineral phases, which could contribute to the OH spectra of the wolframite samples. Given the strong band pleochroism as well as the overall spectral shape, adsorbed moisture, causing in the classical case the appearance of a single non-pleochroic very broad band centred at 3400 cm^{-1}, could be excluded for lack of any such

phenomena in the measured impurity-free zones. Considering the RRUFF database (Downs 2006) we found no spectra showing similar patterns in the OH stretching vibrational region of secondary hydrous mineral phases which could be associated with wolframite, or which have a structural relationship to wolframite. From these observations and also the established correlation of the OH groups contents with the sample chemical composition, we conclude that the identified hydrogen traces represent solely intrinsic point defects in the crystal lattice of wolframite.

The different intensity ratios of the two band groups in different samples of wolframite along with the slightly different polarization behavior indicate two different types of OH groups strongly related to the structural characteristics of wolframite. The monoclinic crystal structure of wolframite (space group *P*2/*c*), can be described in terms of infinite zig-zag chains of XO_6 (X = Fe,Mn,Mg) and WO_6 octahedral groups, which follow the direction of the *c* axis. Each WO_6 octahedron shares two edges with two other WO_6 octahedra and four corners with four XO_6 octahedra which belong to four different XO_6 chains. Cations are surrounded by two crystallographically different oxygen atoms O1 and O2, which occupy a general position; W is coordinated by four O1 and two O2, X by two O1 and four O2 oxygen atoms. From the two oxygen positions, O1 is coordinated by two W and one X atom and O2 by one W and two X atoms in form of a distorted triangle (see Fig. 10).

On the basis of the pleochroic scheme of the OH dipoles and by considering simple crystal chemical rules of cation repulsion, a geometrically and crystal chemically plausible incorporation model of OH point defects into the structure of wolframite can be provided even with full occupancy of all cation positions. Such a model is strongly supported by the positive correlation of the H_2O I contents with $Nb_2O_5 + Ta_2O_5$ (Fig. 9). The two types of pentavalent cations replace W^{6+} at a molar ratio almost precisely 1:1 (Fig. 1). The substitution $W^{6+} + O^{2-} \leftrightarrow (Nb,Ta)^{5+} + OH^-$ thus seems to be one of the mechanisms for the incorporation of a hydroxyl

anion into the structure of wolframite. Different behavior, however, is evident for H_2O II, which does not show any correlation with Nb and Ta. The different behavior suggests that H_2O I is present directly as part of the $(Nb,Ta)O_5(OH)$ octahedra, whereas H_2O II most probably belongs to $WO_5(OH)$ polyhedra situated in the vicinity of 'hydrogen-free' $(Nb,Ta)O_6$ octahedra providing the necessary charge compensation. Another plausible explanation, accounting for the virtually non-existant correlation between H_2O II and the sample chemistry would be a Schottky-type defect $(Fe,Mn,Mg)^{2+} + 2O^{2-} \leftrightarrow V_{Fe,Mn} + 2OH^-$, in which compensation for the lesser negative charge of two OH groups is provided by a vacancy on the bivalent cation site.

One may speculate that rather the presence of trivalent Fe and Mn as part of the substitution mechanism $M^{3+} + (Nb^{5+},Ta^{5+}) \leftrightarrow M^{2+} + W^{6+}$ (M = Fe,Mn) provides the necessary charge compensation for the replacement of W^{6+} by pentavalent Nb and Ta, rather than OH^- replacing O^{2-}. Taking into account the very high difference in H_2O and related (Nb_2O_5+Ta_2O_5) contents of several orders of magnitude (with Nb_2O_5+Ta_2O_5 ranging up to around 30000 wt·ppm in respect to corresponding H_2O contents of but 350 wt·ppm), we consider both charge-compensating mechanisms to be present simultaneously without competing against each another.

In this manner, partial oxidation of Fe and Mn upon sample heating most probably ensures ongoing charge balance in respect to the replacement of W^{6+} by lesser-valent Nb^{5+} and Ta^{5+}, even after the hydrogen has been expelled from the sample at high temperature under the oxidative atmosphere.

The strong pleochroism of the high- and low-energetic bands in (010) with an absorption maximum tilted by an angle of about 110° from the *c* axis requires an orientation of the OH dipole approximately parallel to a line connecting O1 and O2 and/or O1 and O1 oxygen atoms of the WO_6 octahedral units. However, the pleochroism of these bands in (100) with a stronger component parallel to the *b* axis indicates a distinct deviation of the OH vector direction from an

383 alignment within the (010) plane (Fig. 8). This deviation results in a perfect agreement with an
384 OH dipole direction parallel to the O2-O1 and O1-O1 edges of the WO_6 structural units. Usually
385 OH dipole directions are oriented approximately perpendicular to the coordinating cation plane.
386 Due to the large differences in the valences between the coordinating (Mn^{2+}, Fe^{2+}) and (W^{6+},
387 Nb^{5+}, Ta^{5+}) cations and the resulting different repelling of the H atom, deviations from the
388 'normal' to the coordination plane should be expected.
389 The presence of high- and low-energetic bands with a different thermal behavior, a
390 different response to deuteration, along with a different correlation behavior between the
391 (Nb_2O_5+Ta_2O_5) and the H_2O contents, suggest that at least two types of OH positions exist
392 simultaneously in the structure of wolframite and confirm a model that OH defects partially
393 replace the O1 and O2 oxygen atoms. Fig. 10 shows in a schematic diagram the probable OH
394 defect orientation on the O1 and O2 oxygen sites.
395 Considering the correlation diagram of Libowitzky (1999) between the O-H stretching
396 frequencies and O-H···O bond lengths, the mean positions of the high- and low-energetic band
397 groups centered around 3400 and 3100 cm^{-1}, respectively, would require O-H···O bond distances
398 of about 2.8 and 2.7 Å, respectively. With regard to the structures of ferberite and hübnerite,
399 several O-O distances fall into the given range. However, in addition to the interatomic distance,
400 one must also take into account the structural orientation of the given O-O vectors in respect to
401 the observed pleochroic scheme of the OH-stretching IR bands. The direction of maximum
402 absorption of all bands observed on a (010) plate is oriented at about 110° to the *c* axis (Fig. 6,
403 Fig. 8a). All bands show maximum absorption along the *b* axis when viewed along [100] (Fig. 6,
404 Fig. 8b). Considering both the criteria of proper orientation of the O-O vector as well as a
405 plausible interatomic distance, only two hydrogen incorporation sites in the structure of
406 wolframite remain to be considered. Both possibilities represent edges of the WO_6 polyhedra.

The O2- O1 edge with a length of 2.869 Å in the ideal structure of hübnerite is in fair agreement with the expected O-O distance values (Weitzel 1976). The O1- O1 distance amounts to a similar value of 2.865 Å; the value of 2.7 Å derived from the correlation diagram for the low-energetic band group probably indicates local distortion around the OH defects on the O1 site.

The strong correlation between the H_2O content related to the high-energetic OH bands and the (Nb+Ta) content (see Fig. 9) suggests a nearly complete replacement of W by Nb and Ta on the single W site contributing to the coordination of the donor O2 atom in the case of the presumed O2-H···O1 defect (Fig. 10). The low-energetic band group is assigned to OH groups partially replacing O1 oxygen atoms which are coordinated by two W atoms and one *M* position (*M* = Fe, Mn). In this case the O1 oxygen atom acts as the donor oxygen of an O1-H···O1 bond (Fig. 10). One hypothesis explaining additional splitting of the OH stretching IR bands would be the variable occupancy of the cation sites, which coordinate the donor oxygen atoms, by Fe, Mn or Mg. Such interpretation was well established i.e. for amphiboles (Burns and Strens 1966).

Noteworthy is the difference in band resolution and sharpness between pure hübnerite samples, such as #1345 and Fe-containing crystals displaying a significantly larger FWHM of the individual bands, where band separation is noticeable only after cooling the samples down to 80 K (Fig.4). This difference can be explained by the well-established dependence of increasing band FWHM in vibrational IR- and Raman spectra in case of structural disorder provoked either by chemical substitutions (Nasdala et al. 2004, Ruschel et al. 2012) or radiation damage (Nasdala et al. 2001, Ruschel et al. 2012). In this case, the structure of pure hübnerite, with nearly all cation sites occupied by Mn^{2+}, is expected to be much less distorted than in the case of the albeit homovalent $Fe^{2+} \leftrightarrow Mn^{2+}$ substitution, responsible for the broadening of the bands in samples containing both of these elements in significant amount.

Implications

Naturally occurring minerals of the wolframite group represent one of the most important sources of tungsten and their synthetic analogues are of great technological importance, receiving rapidly growing attention as powerful, and at the same time environmentally friendly, photocatalysts, assisting in the decomposition of organic contaminants in both water and air, as well as for scintillation detectors. However, the presence of OH in in ppm concentrations may strongly impact the catalytic and luminescence-emission properties and therefore, worsen the performance of the corresponding devices. Not only do they present an environmentally friendly alternative to other such agents, but can also be synthesized without the use of harmful solvents.

This study showed that hydrous defects in the form of OH groups commonly present in the structure of wolframite-type compounds, in concentrations ranging from 70 up to nearly 450 ppm in the examined natural wolframite samples. Based on the current findings, the incorporation of hydrogen is strongly dependent on the content of pentavalent Nb and Ta in the host tungstate.

The Mg, Fe, Mn and Zn tungstate photocatalysts as well as the luminescent materials are prepared by sol-gel techniques, hydrothermal synthesis or precipitation from aqueous solutions, making the incorporation of hydrogen highly probable. Hence, the presented results on the incorporation mode of hydrous defects in these tungstates, albeit derived from the study of natural wolframite single crystals, are of utmost importance, showing not only how often OH groups enter such compounds and how to identify and quantify them from IR spectra, but also how to manipulate their contents by controlling the presence of pentavalent elements in the hydrothermal batches, even allowing to refine the shape of the obtained nanoparticles to the desired needs.

Acknowledgements

Mg-enriched wolframite samples CET and OLH from Czech metagreisens were kindly provided to us by L. Losertova. Sample 12767 was obtained from the mineral collection of the Institut für Mineralogie und Kristallographie, Universität Wien, all other samples from the mineral collection of the Department of Geological Sciences, Masaryk University. We are indebted to G. Giester for the initial orientation of the wolframite crystals and A. Wagner for subsequent careful sample preparation. We thank B. Mihailova, H. Skogby and an anonymous reviewer for their helpful comments, which enabled us to significantly improve the quality of this paper.

References cited

Bell, D.R., Rossman, G.R., Maldener, J., Endisch, D., and Rauch, F. (2004) Hydroxide in kyanite: A quantitative determination of the absolute amount and calibration of the IR spectrum. American Mineralogist, 89, 998-1003.

Beran, A., and Zemann, J. (1971) Messung des Ultrarot-Pleochroismus von Mineralen. XI. Der Pleochroismus der OH-Streckfrequenz in Rutil, Anatas, Brookit und Cassiterit. Tschermaks Mineralogische und Petrographische Mitteilungen, 15, 71-80 (in German).

Beran, A., Langer, K., and Andrut, M. (1993) Single crystal infrared spectra in the range of OH fundamentals of paragenetic garnet, omphacite and kyanite in an eclogitic mantle xenolith. Mineralogy and Petrology, 48, 257-268.

Beran, A., Talla, D., Losos, Z., and Pinkas, J. (2010) Traces of structural H_2O molecules in baryte. Physics and Chemistry of Minerals, 37, 159-166.

Burns, R.G., and Strens, R.G.J. (1966) Infrared study of hydroxyl bands in clinoamphiboles. Science, 153, 890-892.

Cid-Dresdner, H., and Escobar, C. (1968) The crystal structure of ferberite, $FeWO_4$. Zeitschrift für Kristallographie, 127, 61-72.

Downs, R.T. (2006) The RRUFF Project: an integrated study of the chemistry, crystallography, Raman and infrared spectroscopy of minerals. Program and Abstracts of the 19th General Meeting of the IMA in Kobe, Japan, O03-13.

Ferenc, S., and Uher, P. (2007) Magnesian wolframite from hydrothermal quartz veins in the Rochovce granite exocontact, Ochtiná, Western Carpathians, Slovakia. Neues Jahrbuch für Mineralogie, Abhandlungen, 183, 165-172.

Guha Thakurta, S.R., and Dutta, A.K. (1980) Electric and thermoelectric properties of wolframite $(Fe,Mn)WO_4$ crystals. Bulletin de Minéralogie, 103, 27-32.

Guillen, R., and Regnard, J.R. (1985) Magnetic Properties of Natural and Synthetic Wolframites $Fe_xMn_{1-x}WO_4$. Physics and Chemistry of Minerals, 12, 246-254.

Jingwen, M., Yanbo, C., Maohong, C., and Pirajno, F. (2013) Major types and time-space distribution of Mesozoic ore deposits in South China and their geodynamic settings. Mineralium Deposita, 48, 267-294.

Johnson, E.A. (2006) Water in nominally anhydrous crustal minerals: Speciation, concentration and geologic significance. In: H. Keppler and J.R. Smyth, Eds., Water in Nominally Anhydrous Minerals. Reviews in Mineralogy and Geochemistry, 62, p. 117-154.

Koch-Müller, M., and Rhede, D. (2010) IR absorption coefficients for water in nominally anhydrous high-pressure minerals. American Mineralogist, 95, 770-775.

Lalić, M.V., Popović, Z.S., and Vukajlović, F.R. (2011) Ab initio study of electronic, magnetic and optical properties of $CuWO_4$ tungstate. Computational Materials Science, 50, 1179-1186.

Libowitzky, E. (1999) Correlation of O-H stretching frequencies and O-H…O hydrogen bond lengths in minerals. Monatshefte für Chemie, 130, 1047-1059.

Libowitzky, E., and Beran, A. (2004) IR spectroscopic characterisation of hydrous species in minerals. In: A. Beran, E. Libowitzky, Eds., Spectroscopic Methods in Mineralogy. EMU Notes in Mineralogy, Vol 6. Eötvös Univ Press, p. 227-279.

—— (2006) The structure of hydrous species in nominally anhydrous minerals: Information from polarized IR spectroscopy. In: H. Keppler, J.R. Smyth, Eds., Water in Nominally Anhydrous Minerals. Reviews in Mineralogy and Geochemistry, 62, p. 29-52.

Libowitzky, E., and Rossman, G.R. (1996) Principles of quantitative absorbance measurements in anisotropic crystals. Physics and Chemistry of Minerals, 23, 319-327.

—— (1997) An IR absorption calibration for water in minerals. American Mineralogist, 82, 1111-1115.

Libowitzky, E., Beran, A., Wieczorek, A.K., and Wirth, R. (2012) On the presence of a hydrous component in a gemstone variety of intermediate olivine-type triphylite-lithiophilite, $Li(Fe,Mn)PO_4$. Mineralogy and Petrology, 105, 31-39.

Losertová, L., Houzar, S., Buřival, Z., and Losos, Z. (2012) Wolframite in heavy fraction from the Trucbába - Valcha locality, Moldanubicum. Acta Musei Moraviae, Scientiae Geologicae, 97, 77-84 (in Czech).

Losertová, L., Buřival, Z., Losos, Z., and Houzar, S. (2013) Mineral assemblages and chemical composition of Mg-wolframite and scheelite from Cetoraz near Pacov, Czech Republic. Acta Musei Moraviae, Scientiae Geologicae, 98, 41-48 (in Czech).

Losertová, L., Buřival, Z., and Losos, Z. (2014) Mineral assemblage of Sn-W ores from Ovesná Lhota near Světlá nas Sázavou, Czech Republic. Acta Musei Moraviae, Scientiae Geologicae, 99, 69-76 (in Czech).

549 Losos, Z., and Beran, A. (2004) OH defects in cassiterite. Mineralogy and Petrology, 81, 219-
550 234.
551

552 Miyawaki, R., Yokoyama, K., Matsubara, S., Furuta, H., Gomi, A., and Murakami, R. (2010)
553 Huanzalaite, $MgWO_4$, a new mineral species from the Huanzala mine, Peru. Canadian
554 Mineralogist, 48, 105-112.
555

556 Nasdala, L., Beran, A., Libowitzky, E., and Wolf, D. (2001) The incorporation of hydroxyl
557 groups and molecular water in natural zircon ($ZrSiO_4$). American Journal of Science, 301, 831–
558 857.
559

560 Nasdala, L., Smith, D.C., Kaindl, R., and Ziemann, M., (2004) Raman spectroscopy: analytical
561 perspectives in mineralogical research. In: Beran, A. and Libowitzky, E. (Eds.), Spectroscopic
562 Methods in Mineralogy, EMU Notes in Mineralogy 6, European Mineralogical
563 Union, pp. 281–343.
564

565 Paterson, M.S. (1982) The determination of hydroxyl by infrared absorption in quartz, silicate
566 glasses and similar materials. Bulletin Minéralogique, 105, 20-29.
567

568 Redfern, S.A.T, Bell, A.M.T, Henderson, M.B., and Schofield, P.F. (1995) Rietveld study of the
569 structural phase transition in the sanmartinite ($ZnWO_4$)-cuproscheelite ($CuWO_4$) solid solution.
570 European Journal of Mineralogy, 7, 1019-1028.
571

572 Rudnick, R.L., and Gao, S. (2004) Composition of the continental crust. In: R.L. Rudnick, Ed.,
573 The Crust, 3, p. 1-64.

Ruschel, K., Nasdala, L., Kronz, A., Hanchar, J.M., Többens, D.M., Škoda, R., Finger, F., Möller, A., (2012) A Raman spectroscopic study on the structural disorder of monazite—(Ce). Mineralogy Petrology, 105, 41–55.

Ryskin, Y.I. (1974) The vibrations of protons in minerals: hydroxyl, water and ammonium. In: V.C. Farmer, Ed., The Infrared Spectra of Minerals. Mineralogical Society, London, p. 137-181.

Rossman, G.R. (2006) Analytical methods for measuring water in nominally anhydrous minerals. In: H. Keppler, J.R. Smyth, Eds., Water in Nominally Anhydrous Minerals. Reviews in Mineralogy and Geochemistry, 62, p. 1-28.

Talla, D., Beran, A., Škoda, R., and Losos, Z. (2011) On the presence of OH defects in the zircon-type phosphate mineral xenotime, (Y,REE)PO_4. American Mineralogist, 96, 1799-1808.

Talla, D., Wildner, M., Beran, A., Škoda, R., and Losos, Z. (2013) On the presence of hydrous defects in differently coloured wulfenites ($PbMoO_4$): an infrared and optical spectroscopic study. Physics and Chemistry of Minerals, 40, 757-769.

Wei, W., Hu, R., Bi, X., Peng, J., Su, W., Song, S., and Shi, S. (2012) Infrared microthermometric and stable isotopic study of fluid inclusions in wolframite at the Xihuashan tungsten deposit, Jiangxi province, China. Mineralium Deposita, 47, 589-605.

Weitzel, H. (1976) Kristallstrukturverfeinerung von Wolframiten und Columbiten. Zeitschrift für Kristallographie, 144, 238-258 (in German).

Captions to figures

Figure 1. The negative correlation between W and (Nb+Ta), observed through electron microprobe measurements. The overall trend of the data points aligns nearly perfectly with the substitution vector $W_1 \leftrightarrow (Nb+Ta)_1$ (dashed line). The error bars indicate the 2Sigma values of the EMPA measurements.

Figure 2. Polarized FTIR spectra of selected wolframite samples representing four characteristic types of OH spectra, measured on (010) faces, with the electric vector **E** of the polarized radiation vibrating parallel to the direction of maximum absorption. The spectrum of the hübnerite-dominated sample #5730 is characterized by relatively broad absorption bands around 3400 and 3100 cm^{-1}, that of the hübnerite-dominated sample #5725 shows a single band around 3400 cm^{-1}. The ferberite-rich sample #12767 is characterized by a single broad band around 3100 cm^{-1}. The spectrum of pure hübnerite (#1345) shows relatively sharp bands at 3370 and 3250/3100 cm^{-1}.

Figure 3. Line profile of polarized OH spectra with the **E** vector vibrating perpendicular to the *c* axis measured from the rim to the core of a (010) crystal slab of sample #5725, demonstrating the inhomogeneous distribution of OH defects.

620 **Figure 4.** Polarized FTIR absorption spectra in the OH stretching vibrational region of the
621 hübnerite-dominated sample #1318, (**a**) measured at room temperature, (**b**) measured at 80 K
622 parallel to the *c* axis and parallel to the direction of maximum absorption; the band at 3230 cm^{-1}
623 (asterisk) is due to the formation of ice.
624
625 **Figure 5.** Polarized FTIR spectra in the 3700-2500 cm^{-1} region of the sample #1318, measured
626 parallel to the direction of maximum absorption and parallel to the *c* and *b* axis directions,
627 deconvoluted into single Voigt-shaped bands. Bands at 3420 and 3360 cm^{-1} form the 'high-
628 energetic band group', bands at 3230, 3130, 3040, 2960 and 2870 cm^{-1} form the 'low-energetic
629 band group'. Contaminating C H bands, overlapping low-energetic bands are marked by
630 asterisks.
631
632 **Figure 6.** Polarized FTIR spectra in the 3700-2700 cm^{-1} region of the pure hübnerite sample
633 #1345, measured parallel to the direction of maximum absorption and parallel to the *c* and *b* axis
634 direction, baseline-corrected and deconvoluted into single Voigt-shaped bands. The absorbance
635 scale in (**a**) corresponds to the scaling in Figure 5 to allow comparison; (**b**) depicts in detail the
636 fitted weaker bands. The bands at 3430, 3390, 3370 and 3340 cm^{-1} form the 'high-energetic band
637 group', bands at 3240, 3150, 3080 and 2980 cm^{-1} form the 'low-energetic band group'.
638
639 **Figure 7.** Polarized FTIR spectra of untreated and deuterated wolframite samples measured with
640 **E** vibrating along the direction of maximum absorption (110° to the *c* axis on the (010) crystal
641 slab); (**a**) hübnerite-dominated wolframite sample #5730; deuteration performed at 360 °C, 72 h.
642 The OD bands at 2520 and 2320 cm^{-1} correspond to the OH bands around 3400 and 3100 cm^{-1},
643 respectively. The presence of atmospheric CO_2 causes a band around 2350 cm^{-1} (asterisk),

644 overlapping the OD absorption; (**b**) pure hübnerite sample #1345; deuteration performed at 600
645 °C, 36 h. The OD band at 2495 cm^{-1} corresponds to the prominent 3370 cm^{-1} band, the relatively
646 strong OD band at 2525 cm^{-1} apparently corresponds to the extremely weak OH band at 3430 cm^{-1}
647 . The presence of atmospheric CO_2 causes a band around 2350 cm^{-1} (asterisk). Note that the
648 spectrum of the deuterated sample refers to the absorbance scale at the right side of the plot.
649
650 **Figure 8.** OH absorption figures plotted as values of linear absorption coefficients α in cm^{-1} of
651 selected high- and low-energetic bands, which represent the pleochroic behavior of all
652 deconvoluted bands; (**a**) the upper figure shows the absorption behavior of the bands at 3420,
653 3230 and 3130 cm^{-1} on a (010) crystal plate of wolframite sample #5730, the lower figure shows
654 the absorption behavior of these bands on a (100) plate; (**b**) the upper figure shows the absorption
655 behavior of the bands at 3370, 3340 and 3240 cm^{-1} on a (010) crystal plate of pure hübnerite
656 (sample #1345), the lower figure shows the absorption behavior of these bands on a (100) plate.
657 Note the different expansion scales of the plotted absorption coefficients.
658
659 **Figure 9.** Positive correlation between (Nb_2O_5+Ta_2O_5) and the IR spectroscopically determined
660 H_2O I contents.
661
662 **Figure 10.** The wolframite structure viewed along the *b* axis, demonstrating the proposed OH
663 defect incorporation model for a partial OH replacement of the O1 oxygen position (case **B**),
664 related to the low-energetic band group around 3100 cm^{-1} in wolframite, respectively 3250/3100
665 cm^{-1} in pure hübnerite, and of the O2 oxygen position, related to the high-energetic band group
666 around 3400 cm^{-1} in wolframite, respectively 3370 cm^{-1} in pure hübnerite (case **A**).
667

668

669

670 **Table captions**

671

672 **Table 1.** Sample ID, sample localities, endmember ratios as calculated from EMP analyses,
673 genetic type and IR spectroscopically determined water concentrations.

674

675 **Table 2.** Electron microprobe analyses showing the average chemical composition of each
676 sample as oxide weight ratios, chemical formula units (apfu) calculated on the basis of 2.0
677 cations, and molar endmember ratios; the relative measurement error for WO_3 is 0.15 wt%; that
678 of FeO, MnO and MgO 0.3 wt%, 0.2 wt% and 0.02 wt%, respectively. Nb_2O_5 and Ta_2O_5 show a
679 standard error of 0.1 and 0.07 wt%, respectively. Other measured oxides (SiO_2, TiO_2, ZnO, CaO,
680 MoO_3, NiO, PbO) were constantly present in amounts well below the detection limit of the
681 instrument and are not shown.

682

683

684

685

686

687

688

689

690

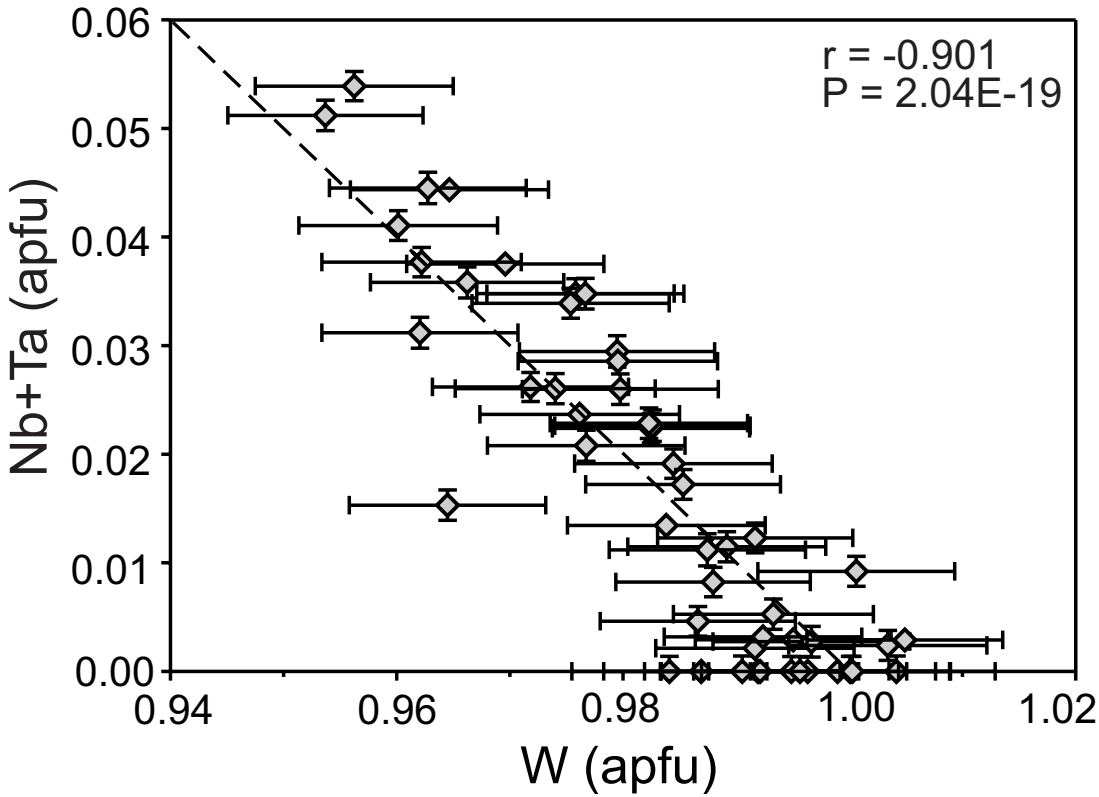
r = -0.901
P = 2.04E-19
Nb+Ta (apfu)
W (apfu)
0.06
0.05
0.04
0.03
0.02
0.01
0.00
0.94
0.96
0.98
1.00
1.02

Figure 1

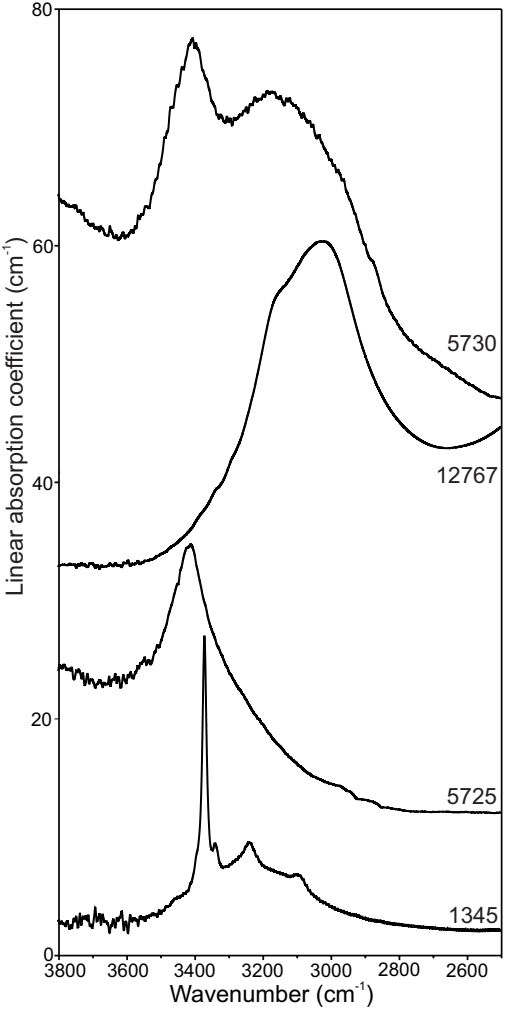
80
60
40
20
0
Linear absorption coefficient (cm-1)
5730
12767
5725
1345
3800
3600
3400
3200
3000
2800
2600
Wavenumber (cm-1)

Figure 2

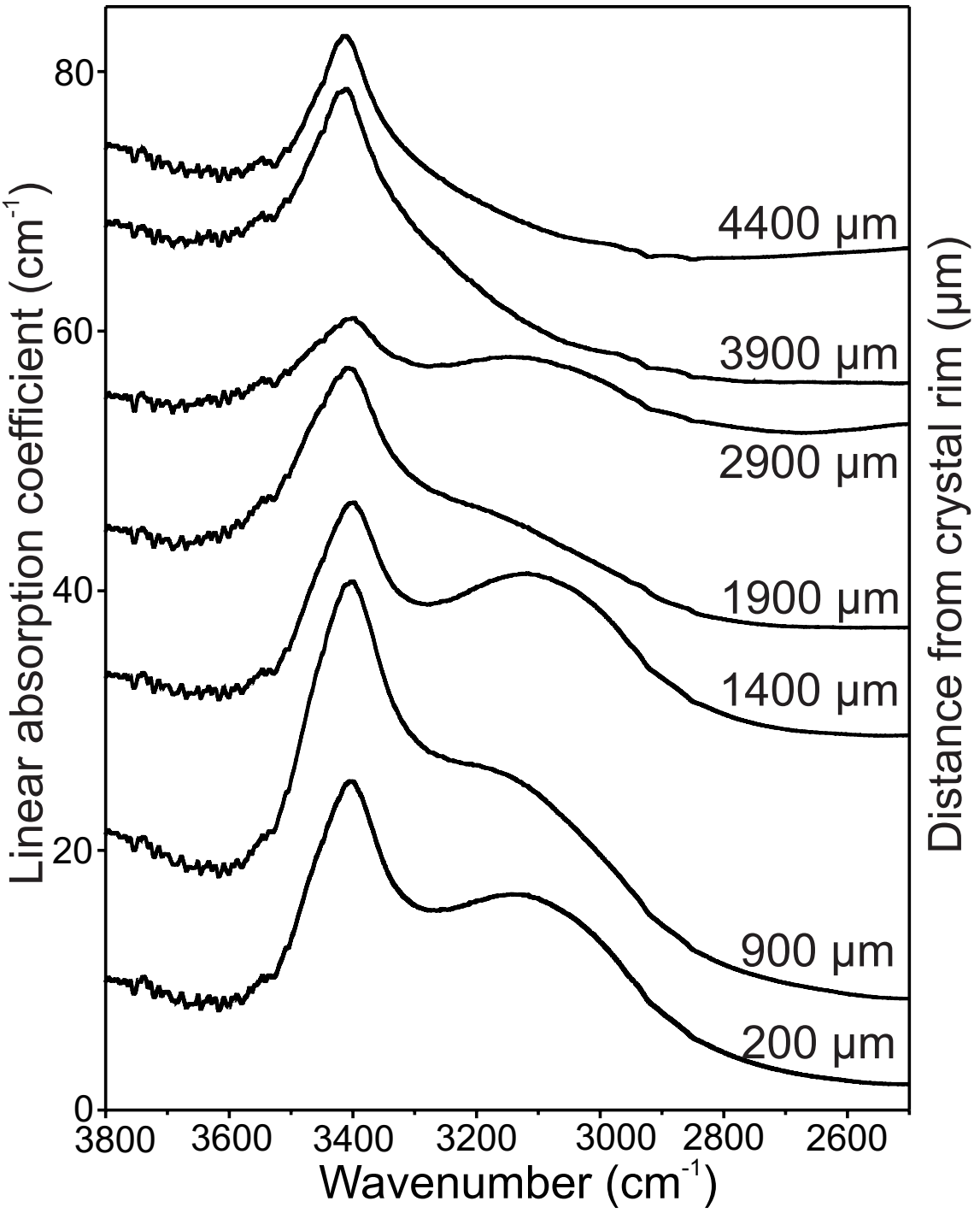
Linear absorption coefficient (cm-1)
Distance from crystal rim (μm)
Wavenumber (cm-1)
0
20
40
60
80
3800
3600
3400
3200
3000
2800
2600
4400 μm
3900 μm
2900 μm
1900 μm
1400 μm
900 μm
200 μm

Figure 3

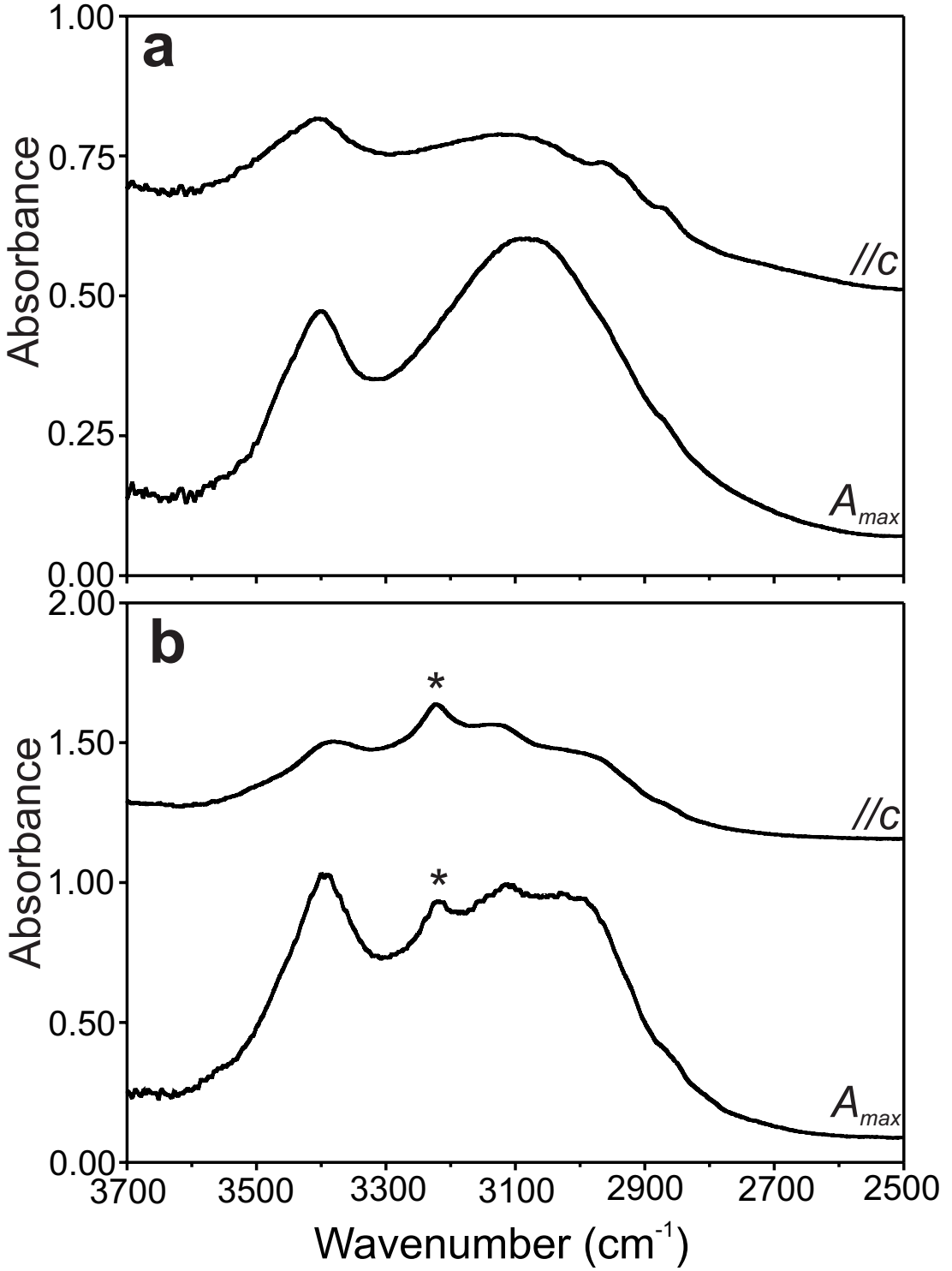
a
b
Absorbance
1.00
0.75
0.50
0.25
0.00
2.00
1.50
1.00
0.50
0.00
//c
A_{max}
*
3700
3500
3300
3100
2900
2700
2500
Wavenumber (cm^{-1})

Figure 4

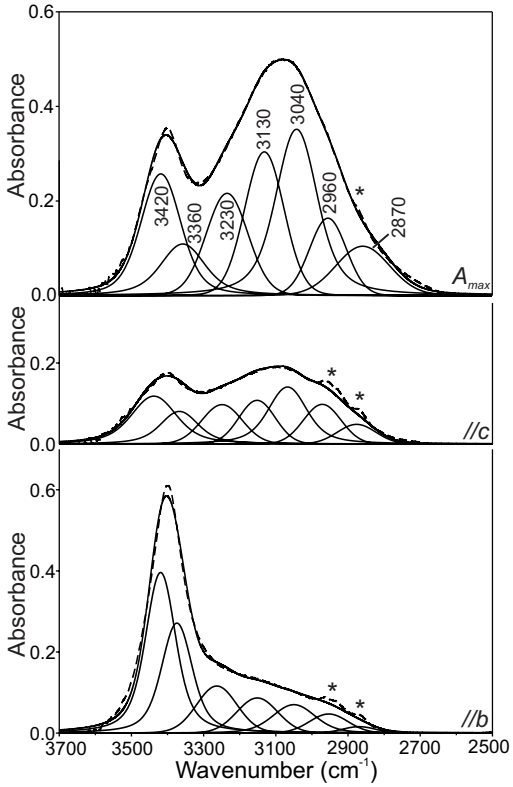
Absorbance
0.6
0.4
0.2
0.0
3420
3360
3230
3130
3040
2960
2870
*
A_{max}
Absorbance
0.2
0.0
*
*
//c
Absorbance
0.6
0.4
0.2
0.0
*
*
//b
3700
3500
3300
3100
2900
2700
2500
Wavenumber (cm^{-1})

Figure 5

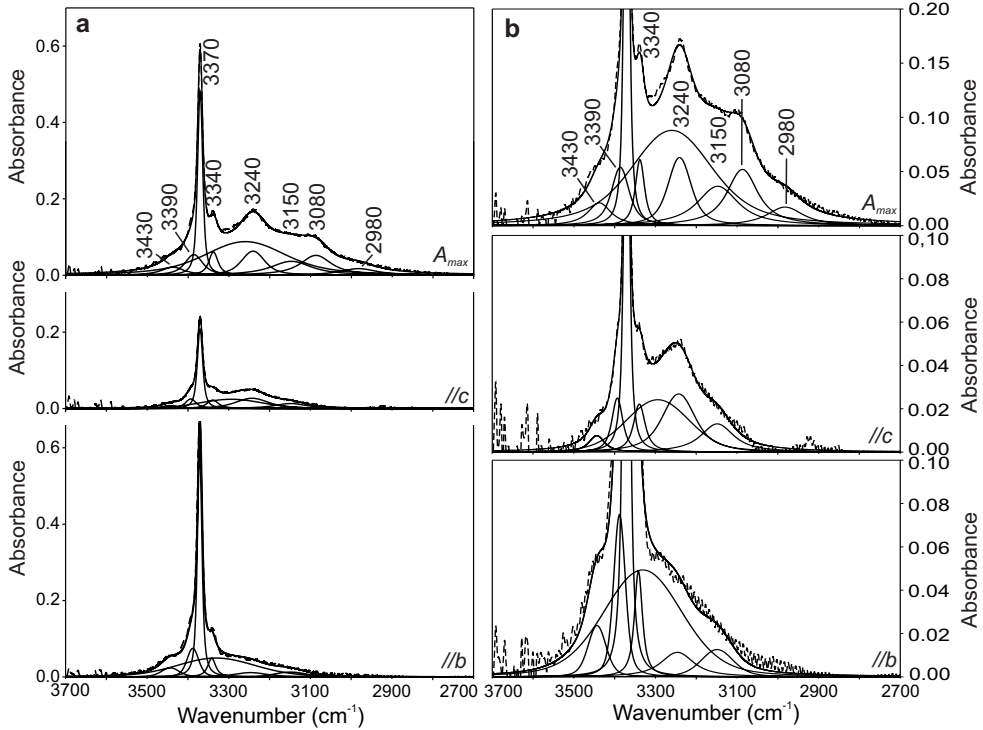
a
b
3430
3390
3370
3340
3240
3150
3080
2980
A_{max}
//c
//b
Absorbance
Wavenumber (cm^{-1})
3700
3500
3300
3100
2900
2700

Figure 6

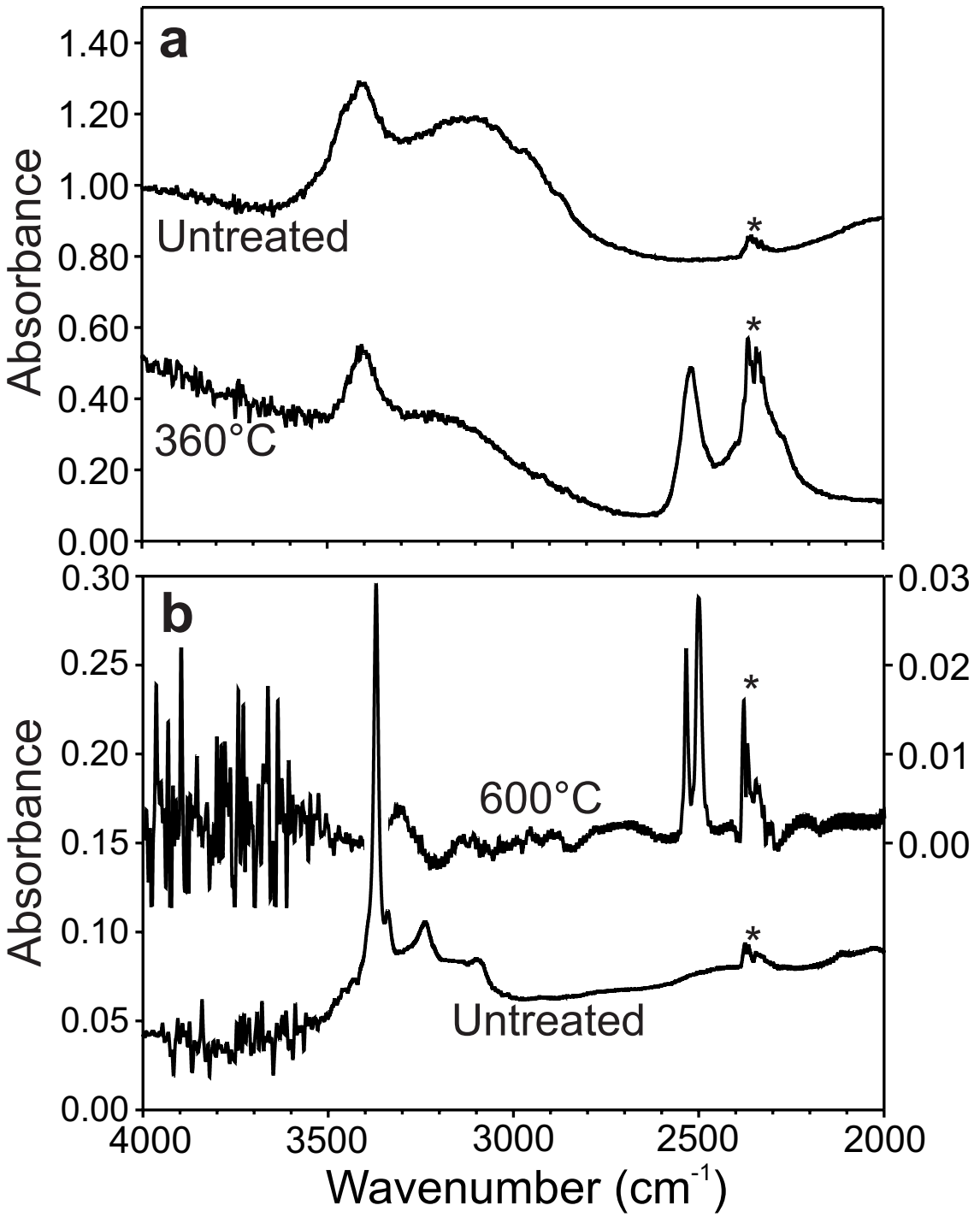
a
b
Absorbance
Untreated
360°C
600°C
Untreated
*
Wavenumber (cm-1)
1.40
1.20
1.00
0.80
0.60
0.40
0.20
0.00
0.30
0.25
0.20
0.15
0.10
0.05
0.00
0.03
0.02
0.01
0.00
4000
3500
3000
2500
2000

Figure 7

Figure 8

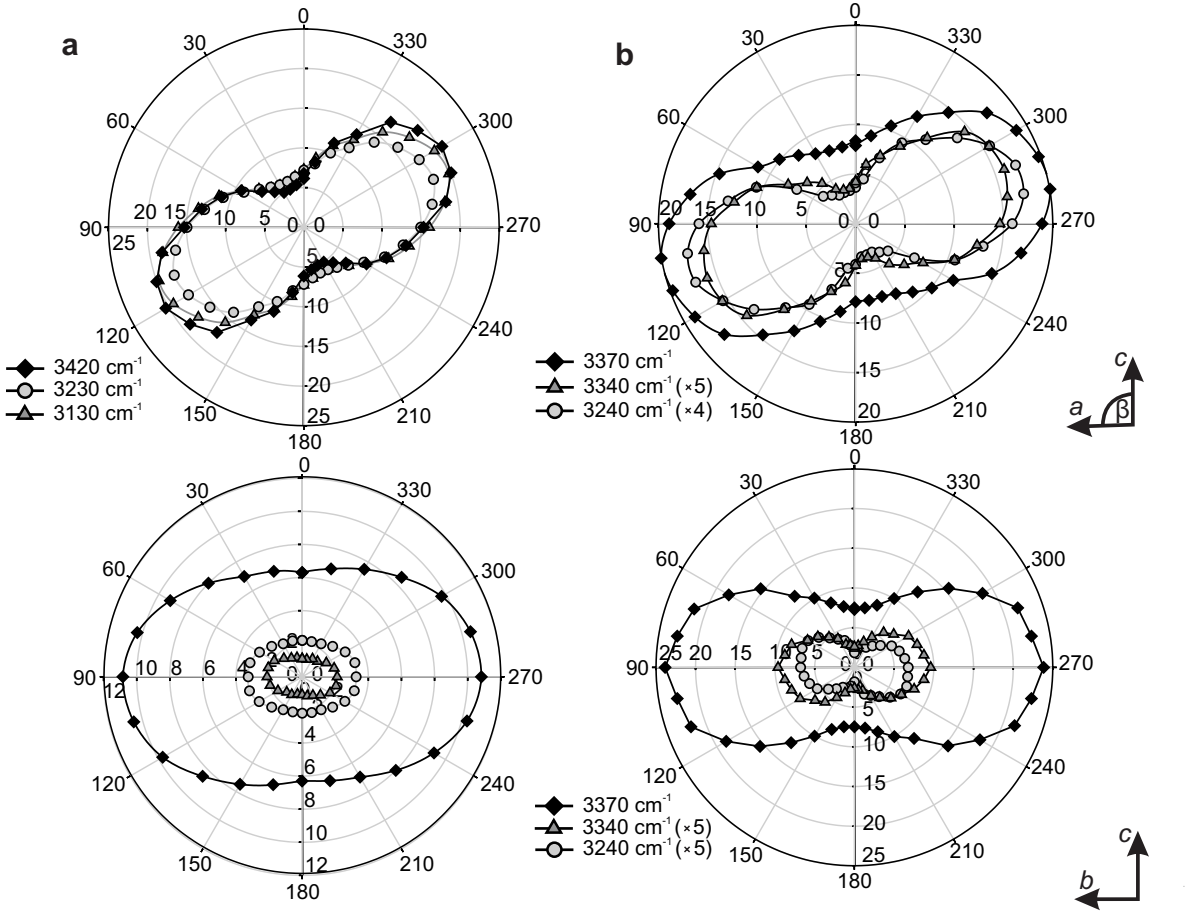
a
b
3420 cm-1
3230 cm-1
3130 cm-1
3370 cm-1
3340 cm-1 (×5)
3240 cm-1 (×4)
3370 cm-1
3340 cm-1 (×5)
3240 cm-1 (×5)
c
a
β
c
b

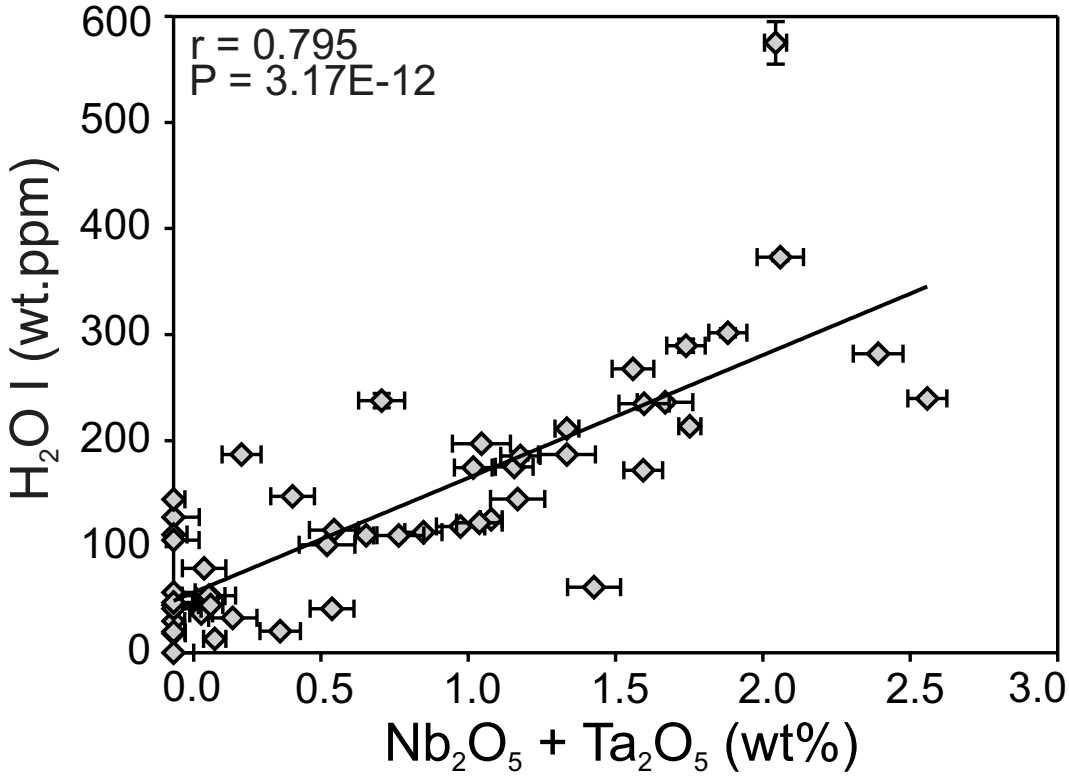
r = 0.795
P = 3.17E-12
600
500
400
300
200
100
0
0.0
0.5
1.0
1.5
2.0
2.5
3.0
H2O I (wt.ppm)
Nb2O5 + Ta2O5 (wt%)

Figure 9

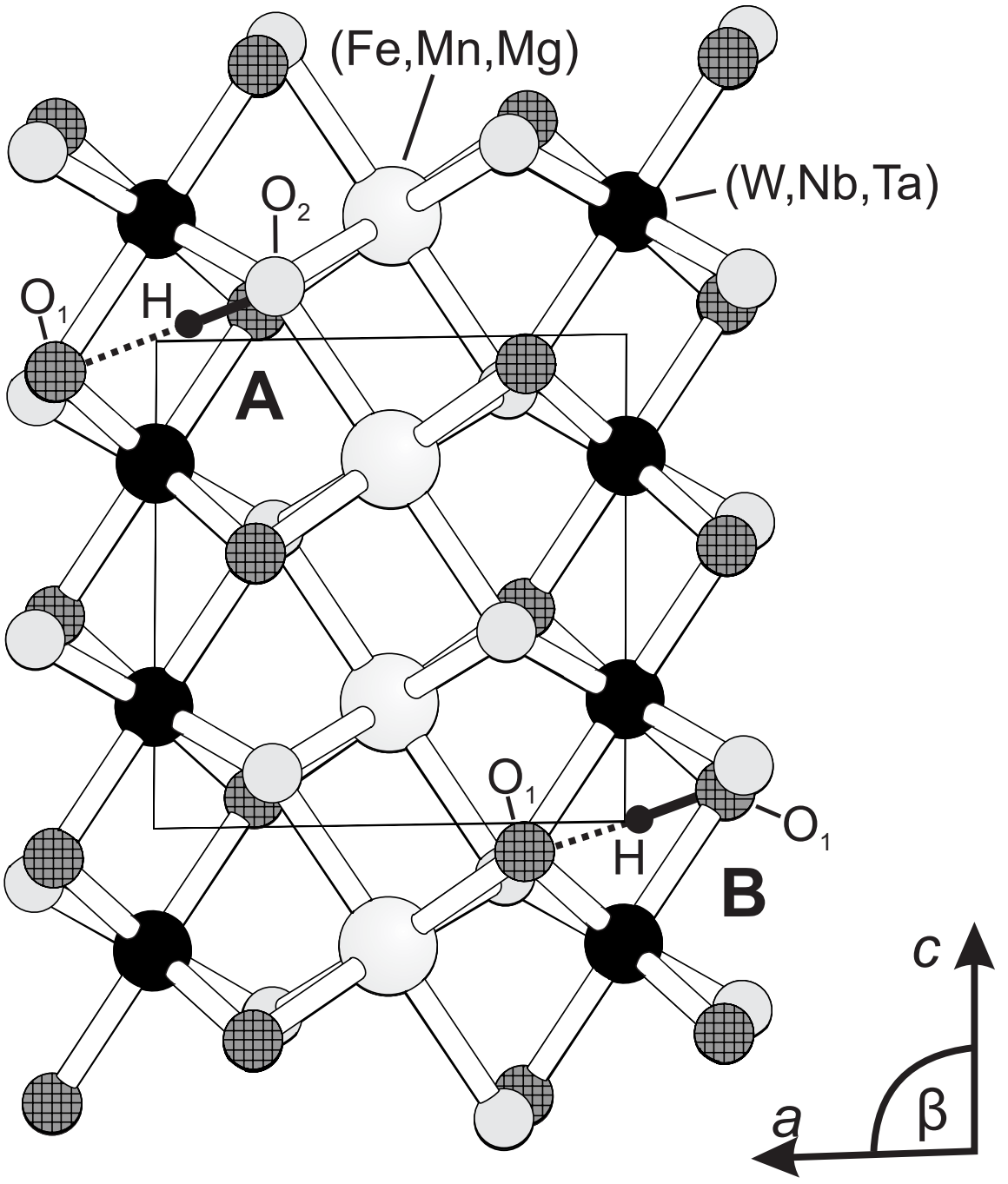

Figure 10

Sample ID	Locality	Endmember ratio (mol %)	W,Nb,Ta (apfu)	Genetic type	H_2O I (wt.ppm)	H_2O II (wt.ppm)	H (w
#1318	Neudorf, Harz, Germany	$Fb_{37}Hb_{63}Hz_0$	$W_{0.98}Nb_{0.019}Ta_{0.000}$	Vein	138	232	
#5735	Los Bonderos, Argentina	$Fb_{38}Hb_{62}Hz_0$	$W_{0.99}Nb_{0.004}Ta_{0.001}$	Vein breccias	81	91	
#5725	Horní Slavkov, Czech Rep.	$Fb_{39}Hb_{61}Hz_0$	$W_{0.98}Nb_{0.027}Ta_{0.002}$	Greisen	207	86	
#5737	Tirpersdorf, Sachsen, Germany	$Fb_{86}Hb_{12}Hz_2$	$W_{0.99}Nb_{0.002}Ta_{0.000}$	Greisen	33	57	
#5721	San Juan, Colorado, USA	$Fb_3Hb_{97}Hz_0$	$W_{0.99}Nb_{0.002}Ta_{0.000}$	Vein	73	67	
#1345	Nevada, USA	$Fb_0Hb_{100}Hz_0$	$W_{0.99}Nb_{0.000}Ta_{0.000}$	Vein	51	35	

#797	Andreasberg, Harz, Germany	$Fb_{75}Hb_{25}Hz_{0}$	$W_{0.97}Nb_{0.021}Ta_{0.002}$	Vein	160	288
#5730	Cínovec, Czech Rep.	$Fb_{37}Hb_{63}Hz_{0}$	$W_{0.97}Nb_{0.033}Ta_{0.003}$	Greisen	233	189
CET	Cetoraz, Czech Rep.	$Fb_{77}Hb_{19}Hz_{4}$	$W_{0.99}Nb_{0.008}Ta_{0.000}$	Metagreisen	53	136
OLH	Ovesná Lhota, Czech Rep.	$Fb_{78}Hb_{19}Hz_{3}$	$W_{1.000}Nb_{0.000}Ta_{0.000}$	Metagreisen	47	27
#12767	Krantzberg mine, Usakos, Namibia	$Fb_{92}Hb_{8}Hz_{0}$	$W_{0.99}Nb_{0.007}Ta_{0.000}$	Pegmatite	32	173

Oxide (wt%)	**Sample ID[a]**										
	#1318(5)	#5735(10)	#5725(10)	#5737(9)	#5721(5)	#1345(3)	#797(5)	#5730(9)	CET(3)	OLH(3)	#12767(3)
FeO	8.9	9.0	9.2	20.5	0.7	bdl	17.7	8.7	18.4	18.8	22.1
MnO	14.8	14.5	14.2	2.8	22.5	23.4	5.8	14.8	4.5	4.5	1.8
MgO	bdl	0.01	bdl	0.34	bdl	bdl	0.01	bdl	0.60	0.34	0.06
Nb_2O_5	0.85	0.16	1.19	0.07	0.11	bdl	0.91	1.45	0.37	bdl	0.32
Ta_2O_5	0.01	0.04	0.14	bdl	bdl	bdl	0.15	0.21	bdl	bdl	bdl
WO_3	76.0	75.9	74.9	76.3	74.9	76.0	74.0	74.4	76.3	76.6	75.9
Formula (apfu)											
Fe	0.37	0.38	0.39	0.86	0.03	0.00	0.75	0.36	0.77	0.79	0.92
Mn	0.63	0.62	0.61	0.12	0.97	1.00	0.25	0.63	0.19	0.19	0.08
Mg	0.000	0.001	0.000	0.025	0.000	0.000	0.001	0.000	0.045	0.025	0.005
Nb	0.019	0.004	0.027	0.002	0.002	0.000	0.021	0.033	0.008	0.000	0.007
Ta	0.000	0.001	0.002	0.000	0.000	0.000	0.002	0.003	0.000	0.000	0.000
W	0.98	0.99	0.98	0.99	0.99	0.99	0.97	0.97	0.99	1.00	0.99

O	4.00	4.00	4.00	3.99	3.98	3.98	3.97	3.99	3.99	3.99	3.98
Endmembers (mol%)											
Ferberite	37.17	37.84	38.96	85.64	3.10	0.00	74.93	36.58	76.51	78.46	91.83
Hübnerite	62.83	62.05	61.04	11.86	96.90	100.00	25.00	63.42	19.05	19.04	7.71
Huanzalaite	0.00	0.11	0.00	2.50	0.00	0.00	0.07	0.00	4.44	2.50	0.46

[a] The number in parantheses indicates the count of analytical points in the given sample.